Controlling the Fold: Proprioceptive Feedback in a Soft Origami Robot

Nathaniel Hanson^{1†}, Immanuel Ampomah Mensah^{1†}, Sonia F. Roberts^{2†}, Jessica Healey¹, Celina Wu¹, and Kristen L. Dorsey^{1*}

Correspondence*: 360 Huntington Avenue, EXP 120, Boston, MA 02120 k.dorsey@northeastern.edu

ABSTRACT

11

- We demonstrate proprioceptive feedback control of a one degree of freedom soft, pneumatically
- actuated origami robot and an assembly of two robots into a two degree of freedom system.
- The base unit of the robot is a 41 mm long, 3-D printed Kresling-inspired structure with six sets
- of sidewall folds and one degree of freedom. Pneumatic actuation, provided by negative fluidic
- 7 pressure, causes the robot to contract. Capacitive sensors patterned onto the robot provide
- position estimation and serve as input to a feedback controller. Using a finite element approach,
- the electrode shapes are optimized for sensitivity at larger (more obtuse) fold angles to improve
- 10 control across the actuation range. We demonstrate stable position control through discrete-time proportional-integral-derivative (PID) control on a single unit Kresling robot via a series of static
- set points to 16 mm, dynamic set point stepping, and sinusoidal signal following, with error under
- 3 mm up to 10 mm contraction. We also demonstrate a two-unit Kresling robot with two degree of
- freedom extension and rotation control, which has error of 1.7 mm and 6.1°. This work contributes
- optimized capacitive electrode design and the demonstration of closed-loop feedback position
- control without visual tracking as an input. This approach to capacitance sensing and modeling
- constitutes a major step towards proprioceptive state estimation and feedback control in soft 17
- origami robotics. 18
- Keywords: origami, soft robotics, flexible electronics, feedback control, capacitive sensor, soft sensor, proprioception

INTRODUCTION 1

- Soft robots may soon be part of daily life, with envisioned applications ranging from helping humans
- Robertson et al. (2021); Wu et al. (2021) to holding fragile objects without causing damage Li et al. (2019). 21
- These robots currently have limited impact outside of the lab Hawkes et al. (2021), but a growing body of
- work is demonstrating the state estimation, position control, and force control Best et al. (2016); Tapia et al. 23
- (2020) that is essential for integrating soft robots into these target applications. 24
- 25 A wide range of approaches are used for position or force sensing; common types are motion capture
- Della Santina et al. (2018); Patterson et al. (2020), pressure sensors external to the actuator Best et al. 26

 $^{^{}m 1}$ Institute for Experiential Robotics, Northeastern University, Boston, USA

²Department of Mathematics & Computer Science, Wesleyan University, Middletown, CT, USA

[†]These authors contributed equally to this work and share first authorship

Fluidic input (behind panel)

Capacitive electrodes

Target setpoint: Contract top face by 14 mm without rotating

Figure 1. (a) The single-unit Kresling robot in the test stand. The capacitive sensors used for proprioception and feedback control are visible on one of three valley fold sets. The retroreflective markers are used only for optical groundtruthing. (b) The vertically stacked, two-unit Kresling robot during a static setpoint test, with target top face contraction of 14 mm with 0° rotation. In contrast to the single-unit robot, this robot has two degrees of freedom with independent contraction and rotation of the top face.

t = 30 s

t = 0 s

(2016), and embodied mechanical sensors Yan et al. (2023). Many scenarios in which feedback controlled soft robots are expected to excel over rigid robots, such as collaboration with humans or use in highly portable applications, present privacy or logistical challenges for motion capture. Pressure sensing is only possible for controlling fluidic actuators, and its accuracy will vary with leaks and tubing size. Additionally, range sensing on deformable objects is subject to interference and misalignments between sensors as the actuators deform. Soft mechanical sensors can both be integrated directly into the robot body and provide accurate force and shape estimations Kim et al. (2021); Dorsey et al. (2022); Sun et al. (2022b); Dong et al. (2022); Thuruthel et al. (2019); Huang et al. (2022); Wang et al. (2022). Improving mechanical sensor performance to achieve closed-loop control will be critical to meet future soft robotics sensing and control needs.

In this work, we demonstrate proprioceptive sensing and feedback control of the pose of single and two degree-of-freedom (DOF) Kresling Kresling (2012) origami robots (Fig. 1). Previous research in Kresling robots has assembled multiple units to form multi degree of freedom arms (Wu et al. (2021); Kaufmann et al. (2022) and crawlers (Ze et al. (2022); Pagano et al. (2017)). These works showcased the potential of open loop controlled multi-unit robots to achieve extension, roll, and pitch at the face of each unit and

- 42 translation and bending at the robot tip. However, closed loop operation will be necessary for operation in
- 43 a range of environments with external forces and non-idealities.
- 44 This work investigates the design of capacitive sensors for robot proprioception and simple feedback control.
- 45 We also show that the Kresling robot approach is compatible with the common soft robotic principles of
- 46 elastomeric material fabrication and fluidic actuation. This work contributes to the state-of-the-art in soft
- 47 robotics proprioceptive control by:
- Designing capacitive position sensors to meet practical mechanical and electrical constraints for soft
 origami feedback control.
- 50 2. Fabricating 3D-printed elastomeric Kresling units to enable fluidic actuation.
- 51 3. Demonstrating feedback control of Kresling robots using only capacitive electrodes, including a two degree of freedom, two-unit robot with independent extension and yaw control.
- Under fluid input of 80 kPA absolute, the single-unit actuator contraction is 75% of its total length (31
- 54 mm). We demonstrate single-unit feedback control to 40% of the extended length (16 mm) and error below
- 4 mm for all setpoints. In the two-unit robot, we demonstrate independent control of the contraction and
- 56 rotation of the top face to 14 mm of contraction and $\pm 16^{\circ}$ of rotation. To our knowledge, this is the first
- 57 demonstration of a soft origami robot with feedback control using only capacitive proprioception.

2 RELATED WORK

- 58 Shih et al. (2020) offer a comprehensive review of the state of soft robotic shape estimation, perception, and
- 59 efforts towards closed loop control. Here, we highlight recent efforts in soft material sensors for actuator
- shape or force estimation using flexible circuit components such as capacitors Kim et al. (2021); Dorsey
- et al. (2022), resistors Sun et al. (2022b); Dong et al. (2022); Thuruthel et al. (2019), or inductors Huang
- 62 et al. (2022); Wang et al. (2022) fixed to the robot body. Detecting the angle between two actuator faces has
- also been well reported Mori and Onoe (2021); Wang et al. (2022), with angle accuracies ranging from 12°
- Mori and Onoe (2021) for a piezoresistive sensor to $\pm 1^{\circ}$ for an inductive sensor Wang et al. (2022). Fold
- angle sensing is particularly advantageous in folded and origami robots, where the mechanical properties
- and deformation of an actuator may be designed through pattern selection and parameters Park et al. (2022)
- 67 and the relationship between fold angles and faces is well-defined.
- Earlier demonstrations of origami robots folded in paper or polymers focused on the ability to reconfigure,
- 69 deploy, or self-assemble by folding or unfolding Robertson et al. (2021); Chen et al. (2022) using actuation
- 70 approaches such as magnetic fields Wu et al. (2021); Ze et al. (2022), fluidic pressure Park et al. (2022);
- 71 Chen et al. (2022), electric fields Li et al. (2018), and tendons Kaufmann et al. (2022). Insight gained
- 72 from these fabrication, actuation, and sensing approaches spurred interest in more complex patterns and
- 73 motions. Origami patterned robots have led to demonstrations as grippers Robertson et al. (2021), crawlers
- 74 Chen et al. (2022); Sun et al. (2022a); Ze et al. (2022), jumpers Sun et al. (2022b), and haptic feedback
- 75 devices Williams et al. (2022). One common design for origami soft robots is the Kresling pattern due to its
- 76 ability to achieve bistable states defined by its pattern geometry and its behavior as a two DOF joint when
- 77 compressed Kresling (2012); Kim et al. (2022); Babu et al. (2023). Prior work has applied the Kresling
- 78 pattern to create crawlers Ze et al. (2022); Pagano et al. (2017) and multi-segment continuum arms under
- 79 magnetic Wu et al. (2021) or cable-driven Kaufmann et al. (2022) actuation.
- 80 In contrast to the wealth of soft mechanics and actuator work present in origami robotics literature,
- 81 position sensing and feedback control research has received less attention. Notable recent work has

investigated the integration of rigid (e.g., photoresistor) or soft mechanical sensors into active origami structures for on-off feedback control. Nisser et al. embedded phototransistors and LEDs in a flat origami 83 structure to control angles during structure self-folding Nisser et al. (2016). Researchers have also integrated 84 contact switches and tactile sensors Yan et al. (2023); Sun et al. (2022a) to enable hysteresis control in 85 jumping, gripping, and crawling soft robots. The uses of soft sensors in this domain include measuring gait 86 and environmental contact in an origami-patterned walker by coating the legs with piezoresistive material 87 Dong et al. (2022), estimating the curvature of a soft finger with a flexible inductor Huang et al. (2022), and 88 controlling the fold of a shape memory alloy in three states with a piezoresistive curvature sensor Firouzeh 89 90 and Paik (2015).

3 STRUCTURE AND MODELING

3.1 Parameters and Kinematic Model

91

- 92 Previous work has thoroughly investigated the mechanics of the Kresling pattern Kaufmann et al. (2022);
- 93 Bhovad et al. (2019). Here, we present a short definition of properties relevant to the modeling of single
- 94 Kresling unit and expand this model to a vertically stacked, two-unit Kresling structure with independent
- 95 heights. Table 1 is a list of all variables and definitions.

Table 1. The Kresling unit properties

Symbol	Meaning	Symbol	Meaning
L	Top length referenced to base	α	Top rotation referenced to base
L_c	Full contraction length	α_c	Full contraction rotation of top face
L_e	Full extension length	α_e	Full extension rotation of top face
L_{2DOF}	2DOF top length referenced to base	α_{2DOF}	2DOF top rotation referenced to base
L_b	Center length referenced to base	α_b	Center rotation referenced to base
L_t	Top length referenced to center	α_t	Top rotation referenced to center
R	Top face radius	ϕ	π / N
N	Number of top face edges	$\mid \dot{\xi} \mid$	Sidewall valley fold angle
λ	Ratio of valley fold to base angle over γ	$ \tilde{\gamma} $	$\pi/2 - \pi/N$

The single-unit structure has one DOF, as described by linked parameters L and α . Four parameters control the morphology: L_c , R, N, and λ . Fig. 2 represents these parameters on the Kresling structure with views (a) in 2D, looking up through the bottom face, and (b) in 3D. These variables are linked by Kaufmann et al. (2022)

$$L = \sqrt{L_c^2 + 2R^2 \left[\cos(\alpha + 2\phi) - \cos(\alpha_c + 2\phi)\right]},\tag{1}$$

100 where $\alpha_c = 2\lambda(\pi/2 - \phi)$.

We will refer to three additional dependent parameters to describe the Kresling structure. At full extension, the structure has length L_e and rotation α_e . Angle ξ is linked to L by finding the angle of intersection between vectors normal to the sidewall triangular faces,

$$n_t = \begin{bmatrix} RL\sin(2\phi)\hat{i} \\ RL\left(1 - \cos(2\phi)\right)\hat{j} \\ R^2\left(\sin(\alpha)(1 - \cos(2\phi)) + (1 - \cos(\alpha))(\sin(2\phi))\right)\hat{k} \end{bmatrix}$$
(2)

104 and

$$n_{b} = \begin{bmatrix} RL(\sin(2\phi - \alpha) + \sin(\alpha))\hat{i} \\ -RL(\cos(2\phi - \alpha) - \cos(\alpha))\hat{j} \\ R^{2}((\cos(2\phi - \alpha) - \cos(\alpha))(\sin(2\phi - \alpha) + \sin(2\phi)))\hat{k} - \\ R^{2}((\cos(2\phi - \alpha) - \cos(2\phi))(\sin(2\phi - \alpha) + \sin(\alpha)))\hat{k} \end{bmatrix}$$
(3)

where \hat{i} , \hat{j} , and \hat{k} are unit vectors on the axes x, y, and z, respectively, such that

$$\cos \xi = \frac{\vec{n}_t \cdot \vec{n}_b}{||n_t|| ||n_b||}.\tag{4}$$

We derived the relationship between L and ξ through Eqs. 1–4. Observing that the relationship between fold angle and length is highly linear via a numerical approach (R^2 of 99.3% in the range of L_c to L_e), we used a linear approximation for the inverse kinematics function

$$L = 0.22\xi + 10.4,\tag{5}$$

109 where ξ is given in degrees.

The two-unit Kresling robot is composed of single units with independent fluidic inputs identical L_c , R, N, and λ parameters, and variable lengths L_t and L_b for the top and bottom units, respectively. The two units are stacked vertically upon one another. The top unit is inverted from the bottom unit such that the center has rotation $\alpha_b = \alpha_e$ and the top face has rotation $\alpha_t = -\alpha_e$ when both top and bottom are fully extended. Actuating only the top unit contracts and rotates the top face clockwise, while actuating only the bottom unit contracts and rotates the top face counterclockwise. Actuating both units results in independent control of contraction and top face rotation with two degrees of freedom.

117 Taking the length from eq. (1) for the top and bottom units, the length from base to top is

$$L_{2DOF} = \sqrt{L_c^2 + 2R^2 \left[\cos(-\alpha_t + 2\phi) - \cos(\alpha_c + 2\phi)\right]} + \sqrt{L_c^2 + 2R^2 \left[\cos(\alpha_b + 2\phi) - \cos(\alpha_c + 2\phi)\right]}, \quad (6)$$

118 while rotation of the top face is $\alpha_{2DOF} = \alpha_t + \alpha_h$.

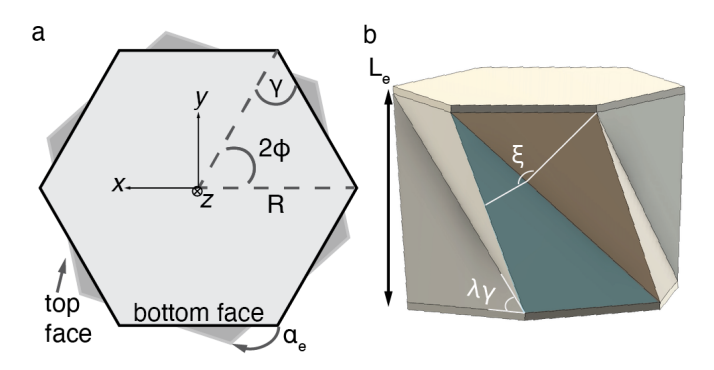


Figure 2. The parameters of the Kresling structure (a) from the bottom face looking up and (b) in 3D. The vector $\vec{n_t}$ is normal to the red shaded face, and the vector $\vec{n_b}$ is normal to the blue shaded face.

3.2 **Position Sensors**

120 Capacitive sensing offers straightforward signal readout with commercial measurement electronics and low

- hysteresis, but the placement of the electrodes must achieve high signal to noise ratio, high sensitivity near 121
- full extension, and robust operation under many extension-contraction cycles. A Kresling unit deforms by 122
- folding at the pattern hinges and contracting, so capacitive sensors could be located on the top and bottom 123
- faces (to measure gap) or the sidewall faces (to measure angle). Placing electrodes on the top and bottom 124
- 125 faces would create a capacitor with a full extension gap of >40 mm and result in a low signal to noise ratio
- near full extension. Electrodes placed on the sidewalls of the Kresling unit would increase signal to noise 126
- ratio over a top-bottom placement but require appropriate selection of shape, size, and orientation to fit on 127
- the triangular pattern faces and to maximize sensitivity. 128
- Existing analytical approximations of the capacitance between angled plates (e.g., Seeger and Boser (2003)) 129
- typically assume the effect of fringing field is negligible and that a small angle approximation is valid. As 130
- the Kresling unit contracts and ξ decreases, the effect of the fringing field on total capacitance will shrink 131
- and the small angle approximation will not accurately describe the full range of contraction. Our initial 132
- tests also showed that the sidewalls flex and twist near the corners, which could cause delamination of the 133
- 134 electrodes from the sidewall. Therefore, we simulated the capacitance change of several electrode shapes
- that did not cover the full sidewall using FEA and compared the sensitivity to a triangular electrode that 135
- covered the sidewall. We wished to model and compare the capacitance change that would occur by moving 136
- near full extension (i.e., L_e) to the capacitance change that would occur by moving near full contraction 137
- (i.e., L_c). Increasing the ratio of capacitance change near full extension over that of capacitance change 138
- near full contraction would improve the signal to noise ratio, so we optimized electrode shape to improve 139
- this ratio. 140
- We optimized the electrode shape in COMSOL Multiphysics (Comsol Inc., v6.0) with a downhill simplex 141
- method Lagarias et al. (1998) implemented in MATLAB (fminsearch, Mathworks, R2021a) through 142
- the Livelink for MATLAB toolbox (Comsol Inc., v6.0). This approach does not rely on an analytical 143
- solution of the gradient (e.g. Newton's method) and was computationally feasible with FEA (e.g., vs. 144
- genetic algorithm). 145
- We constrained electrode size to the area of one triangular sidewall. Each electrode is constructed of the 146
- vertices in the subset x, which is a subset of all potential electrode points in \mathbb{R}^2 bounded by the triangular 147
- sidewall face. Because the potential set of initial conditions is composed of all n-sided polygons, we 148
- 149 constrained the number of vertices to five (to reduce model complexity) and the number of initial conditions
- 150 to five. We chose five initial electrode shapes (ICs) of a hexagon (IC1), a funnel (IC2), triangular and
- inverted triangular shapes (IC 3-4), and an hourglass (IC5). (Fig. 3a) These shapes spanned a large set 151
- 152 of potential electrode shapes for optimization. To halve the model complexity, we enforced a symmetry condition on one sidewall, such that the angle between the triangular face and a horizontal plane is 0.5ξ . 153
- The 0.5ξ value at full extension is approximately 70°, and the value near full contraction is approximately 154
- 10°. We examined the ratio of capacitance change that would occur by moving 5° from full extension (i.e.,
- $\Delta C_{65}(x)$) to the capacitance change that would occur at full contraction (i.e., $C_{10}(x)$). The optimization 156
- function moved the location of the electrode vertices to maximize this ratio $f(x) = \frac{\Delta C_{65}(x)}{C_{10}(x)}$ 157
- Each initial condition reached an optimized condition (OC), and we selected OC5, the electrode with the 158
- largest $\frac{\Delta C_{65}(x)}{C_{10}(x)}$, for experiments. Each $\frac{\Delta C_{65}(x)}{C_{10}(x)}$ is presented in Fig. 3a. Fig. 3b is a plot of the capacitance change $\frac{C-C_{70}}{C_{10}}$ across the full extension to contraction range for each OC and a triangular electrode that covers the sidewall ("triangle"). The $\Delta C_{65}/C_{10}$ for the triangle electrode is 1.07%. 159
- 160
- 161

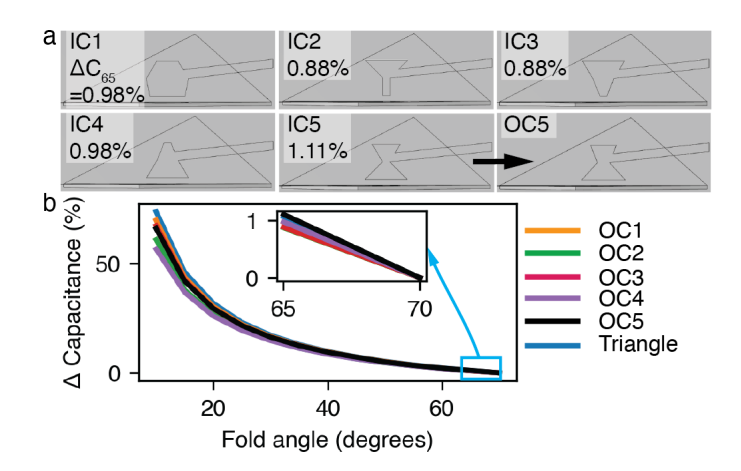


Figure 3. Finite element electrode modeling. (a) The initial electrode shapes IC1-IC5 and OC5. The optimized sensitivities are presented in the top left corners. (b) The simulation results for electrode shapes OC1–OC5 and the triangle electrode. *Inset*: ΔC_{65} .

MATERIALS AND METHODS

4.1 **Fabrication**

162

163

164

165

166

167

168

169

170

171

172

173

175

176

177

178

179

180

181

182

183

184

185

186

187

188

To create an airtight chamber for fluidic actuation, we 3D printed the robot structure in thermal polyurethane (TPU). The TPU permits flexibility of the body and the requisite compliance to twist and contract the structure under the negative fluidic pressures that are commonly demonstrated in soft robotics. Moreover, the TPU is sufficiently nonporous, so it maintains a negative vacuum pressure well. The use of TPU limits the Kresling's stretching at the faces, and we expect its behavior to closely follow kinematic models developed for paper Kresling structures rather than the stretchable and hyperelastic performance of softer materials such as silicone rubbers.

Recent work Wu et al. (2021); Kaufmann et al. (2022) has demonstrated Kresling scales from a single millimeter to over 10 centimeters. Fabrication with a fused deposition modeling 3D printer imposes a practical limit on the scale. The structure's sidewalls must be sufficiently thin to permit repeated contraction, but thick enough that they are reliably printed without leaks. Through experimentation, we determined that a wall thickness of 1 mm was the thinnest wall that delivered a yield above 75% on our equipment 174 without pinholes or porous walls. We chose a scale with a visually obvious stroke between fully contracted and extended states of 2 cm or higher. Finally, the number of structure edges (N) may be four or more. However, a trade-off is present between increasing N and the stiffness of the structure, because more edges require more energy to deform the structure folds.

Taking these factors into account, we fabricated Kresling robots with N=6, R=3 cm, $L_e=4.1$ cm, wall thickness t=1 mm, and $\lambda=0.75$, which correspond to an α_e of 30°. We set the λ value at the midpoint between fully-contracted ($\lambda = 0.5$) and fully-extended ($\lambda = 1$) values. These parameters generate a compliant structure with a maximum extension-contraction stroke of 31 mm.

To fabricate the Kresling robots, we programmatically generated a CAD (Fusion 360, Autodesk) model of the Kresling structure using a custom script that draws the bottom and sidewall faces given the design variables of L, α_e , N, and R and sliced the model for 3D printing with FlashPrint slicer (v.5, FlashForge, v. 5). We 3D printed (Creator Pro 2, Flash Forge) the Kresling structure with TPU filament (NinjaFlex Cheetah 95A) (Fig. 4). Print settings were a 0.4 mm nozzle at an extruder temperature of 238 °C, platform temperature of 40 °C, layer height of 0.18 mm, and print speed of 30 mms⁻¹.

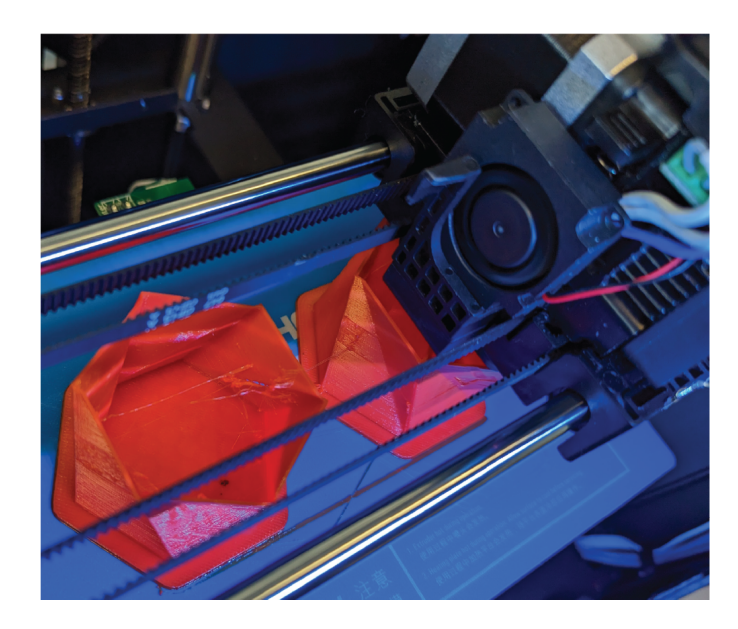


Figure 4. A photograph of the 3D printing process and two Kresling units. The print has progressed halfway.

To form the electrodes, we assembled a stack of copper and nickel plated polyester fabric (woven conductive fabric, 1168, Adafruit) and two-sided adhesive (double-sided adhesive sheets, Michaels, Inc.) with the backing remaining on the back side. We laid this stack onto a cutting mat (Standard Grip mat, Cricut, Inc.) with the back side facing the mat, then cut the electrode stack into the desired shape with an electronic cutting machine and knife blade (Maker 3, Cricut and Cricut Design Space software). We removed the backing from the electrode stack and manually adhered these electrodes to opposite faces of a valley fold using a thin, narrow line extruded on each sidewall during the print step to visually align electrode position. Three capacitors were symmetrically spaced radially around the z axis. Each robot takes approximately three hours to print, adhere the electrodes, and seal.

To actuate and test the robot, we capped the structure with a TPU lid and cyanoacrylate glue (Loctite 495) and inserted pneumatic tubing through holes in the cap. Rigid plastic bases were bonded to the top and bottom faces of the Kresling actuator to enforce rigid bodies for kinematics and optical tracking. These bases also held the measurement cables at known locations relative to the robot. Fig. 1a is a photograph of the robot mounted to a motion capture benchmarking stand.

The two-unit Kresling robot was fabricated with the same approach as the single-unit Kresling through the sealing step. Two individual Kresling units were stacked vertically with individual fluidic inputs for top and bottom units. The junction between the bottom and top unit has two holes for the fluidic inputs to enter the top unit. Two sets of test lead clips were added around this junction to hold half of the test leads for the bottom unit and half of the test leads for the top unit. One set of electrodes was adhered to the top and bottom unit each. These electrodes were measured through two channels on the capacitance to digital board to estimate the contraction of each unit.

4.2 Measurement and Control Setup

Actuator position was driven by a custom fluidic control board and a set of custom ROS Noetic Quigley et al. (2009) nodes that published capacitance, calculated length, and set pulse width modulation (PWM)

values. Data acquisition hardware (LabJack Pro T7) sourced a PWM signal to solenoids (Orange Coast

214 Pneumatics) and the solenoids drove the actuation pressure within the Kresling from 101 kPA (full

- 215 extension) to 80 kPa (full compression) absolute. Communication between the LabJack and ROS was
- enabled through the LabJack library for Linux (2019).
- 217 Capacitance was read at a rate of 90 Hz with a multi-channel capacitance-to-digital converter (FDC2214
- 218 EVM, Texas Instruments), which measures the resonance frequency of a circuit with a known value
- 219 inductor, a known value capacitor, and the sense capacitor in parallel to calculate the capacitance value. In
- 220 the single Kresling unit, capacitance was measured from three sets of electrodes adhered to alternating
- 221 sidewalls and averaged across all three sets for each reading. Although the Kresling robot has six sets
- 222 of sidewalls, we were limited to measurement on three sets for the single-unit robot and two sets for the
- 223 two-unit robot due to limited channels on the measurement electronics.
- 224 To estimate the relationship between L and capacitance, the inverse kinematic model (eq. 5) was combined
- 225 with the FEA model of capacitance (C_{FEA}) vs. ξ (Fig. 3). This relationship was represented as a third-order
- 226 polynomial function in the proprioception and control ROS nodes. Because humidity, local electromagnetic
- 227 fields, and small variations in electrode placement affect capacitance and the match to the FEA model, we
- 228 mapped C_{FEA} to the measured capacitance as $C_{meas} = \kappa^{-1} C_{FEA}$, where κ is a factor that scales C_{meas} .
- 229 We selected a discrete-time implementation of proportional-derivative (PD) control due to its high stability
- 230 and performance in this system. The value of the PWM signal at time t that was fed to the solenoid valves
- 231 on the fluidic control board was

$$PWM_t = PWM_{t-1} + K_p \Delta L + K_d \frac{\Delta L}{\Delta t}$$
(7)

- where PWM_{t-1} is the PWM value of the previous time step, K_p is the proportional gain constant, K_d is
- 233 the derivative gain constant, ΔL is the error between the setpoint and the measured contraction, and Δt is
- 234 the time step. The proportional and derivative gain values were tuned by hand with values of 0.005 and
- 235 0.001, respectively. Before the setpoint was stepped, the single-unit Kresling was set to full extension and
- 236 the initial capacitance was averaged over 5 s. This value is subtracted from subsequent capacitance values
- 237 during the test to de-embed parasitic capacitance due to test cables.
- 238 The center of mass position and rotation of the actuator were measured using a commercial motion
- 239 capture system (V120:Trio OptiTrack, and a custom Optitrack booth and Motive 2.3.7 and Motive 3.0,
- 240 respectively,) that served as the ground truth. Transform coordinate frames (TFs) were sent from Motive
- 241 to ROS for additional processing through a Virtual Reality Peripheral Network (VPRN) interface Bovbel
- 242 (2017).

243

5 RESULTS

5.1 Open-loop Characterization

- We fabricated and compared the sensitivity of electrode OC5 and the triangular electrode by placing
- one set of each electrode type on the sidewalls of the same Kresling. We performed 12 cycles between 0
- 246 mm and 17 mm of contraction (Fig. 5a). Because we cannot directly track fold angle through the motion
- 247 capture system, we present the following results in terms of robot contraction along the z axis.
- The capacitance change per area between 0 mm and 17 mm of contraction is $0.22~\mathrm{pFcm^{-2}}$ and $0.61~\mathrm{mm}$
- pFcm⁻² for the triangular and OC5 electrodes, respectively. While the absolute sensitivity of the triangular
- 250 electrode is higher, the OC5 electrodes yield 2.8 times higher capacitance per unit area.

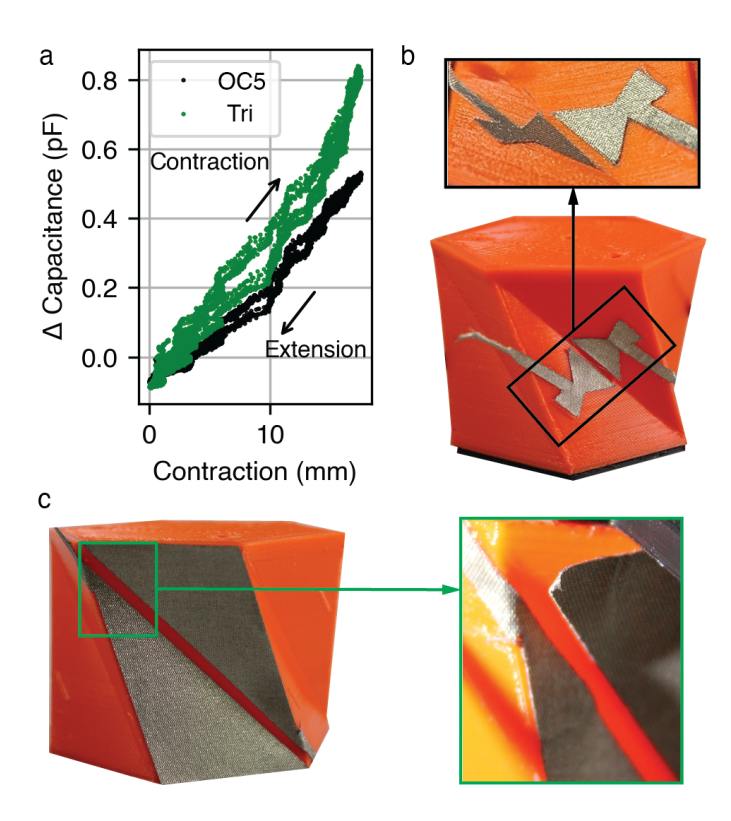


Figure 5. Contraction over 12 cycles to study cyclic loading performance. (a) Capacitance change of the triangular ("Tri.") and optimized OC5 electrodes. (b-c) Photographs of the (b) OC5 and (c) triangular electrodes before actuation. *Insets:* electrodes after actuation. The free end of the OC5 electrode is visible and does not represent delamination.

After cyclic testing, we examined the electrodes for physical degradation. The OC5 electrodes, which sit in the center of the sidewall, showed no delamination from the robot body (Fig. 5b) when compared to the pre-test condition. In contrast, the triangular electrodes wrinkled and delaminated at the corners (Fig. 5c). This delamination was deemed unacceptable because loose electrodes may contact during contraction and yield inaccurate measurements. Therefore, the following tests are presented only with the OC5 electrodes.

We investigated the relationship between L and α for a fabricated Kresling under open loop actuation to determine if the kinematic model that links L and α (i.e., eq. 1) remains valid for Kresling units fabricated in TPU. Fig. 6a is a plot of the kinematic model and measured data for a Kresling unit under open loop actuation from 0 to 17 mm contraction over 90 s. As the contraction increases, the rotation of the top face increases clockwise as predicted by the kinematic model. The root mean square error (RMSE) between measured α and kinematic model α is 1.5°.

During this open loop characterization, we also measured the relationship between contraction and capacitance for a Kresling robot with three sets of OC5 electrodes (S0, S1, and S2) (6b). These values are plot alongside the FEA model prediction for change in capacitance with contraction for OC5, C_{FEA} . As contraction increases, the capacitance between all three sets of electrodes increases, and a difference in sensitivity is observed between the three sets of electrodes. The scales of the measured and modeled capacitance did not align, so we averaged the reading across three electrode sets at each contraction and fit a scale factor κ to this average, with a value of 0.26.

Finally, we measured the capacitance of an electrode set when the Kresling unit was at rest to determine the position error due to noise. Across 14500 samples (120 s of data), the standard deviation was 0.01 pF,

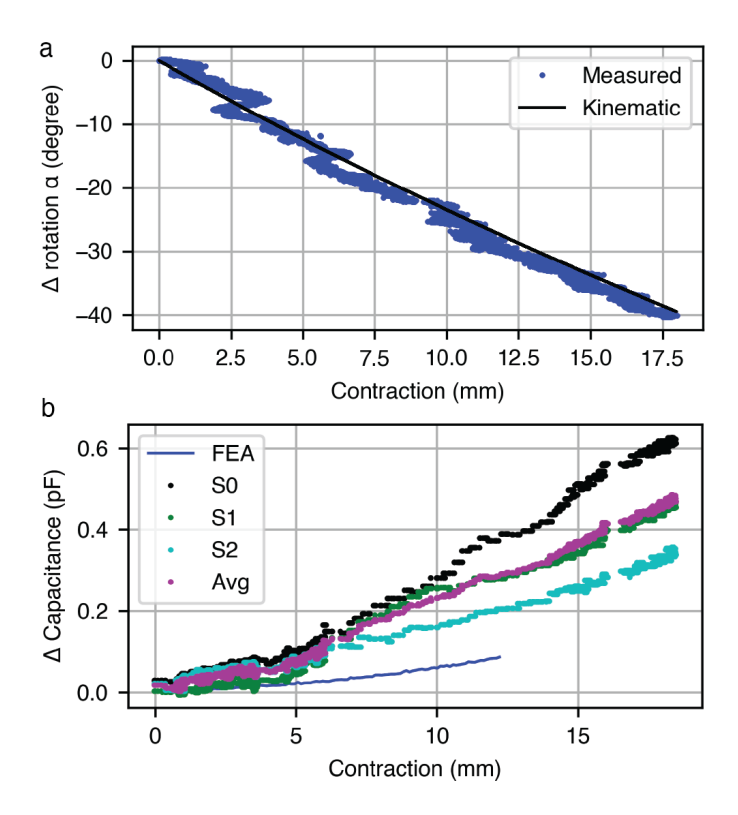


Figure 6. Open-loop response with contraction to verify the kinematic model of a single Kresling actuator. (a) Comparison of the observed Kresling contraction to the top face rotation α using the motion capture setup. (b) For three capacitive electrode pairs on a single Kresling, the measured capacitance change from full extension to full contraction. The average of the three sensor pairs is plotted and compared to the expected performance of the FEA model.

which corresponds to a length error of 1 mm at full extension, or 6% of maximum controlled contraction length.

5.2 Single-unit Feedback Control and Performance Under Load

The setpoint was stepped from full extension to a contracted value under feedback control according to eq. 7. The response of the Kresling robot to multiple commanded setpoints is shown in Fig. 7, including at setpoints of 18 mm, 12 mm, and 6 mm (Fig. 7a-c), time-varying sinusoidal tracking (Fig. 7d), and multiple control setpoints stepped every 30 s (Fig. 7e). RMSE and length are calculated from 20 s to 90 s during the test, and the error bars in Fig. 7c represent standard deviation in length over three tests.

To determine the performance under load, we measured a force-displacement curve (Fig. 7f) to the maximum compressed length of a single-unit Kresling completed with a force testing machine (Mecmesin iTest 2.5kN through Emperor Force software), and placed a 500 g mass on the single-unit Kresling before the setpoint was stepped from 0 mm to a series of setpoints (Fig. 7e, g). The RMSE is 3 mm and the Kresling contracts less than the experiment without the 500 g mass.

5.3 Two-unit Feedback Control

273

274275

276277

278

284

285

286

287

288

To demonstrate two-unit and two DOF Kresling robot control, we we constructed a vertical stack of two Kresling units. This experiment is designed to demonstrate independent control of a multi-DOF Kresling robot, as an exemplar for how larger scale actuation is achievable by chaining together multiple units while still maintaining control of each. The fluidic input for each unit was independent and controlled

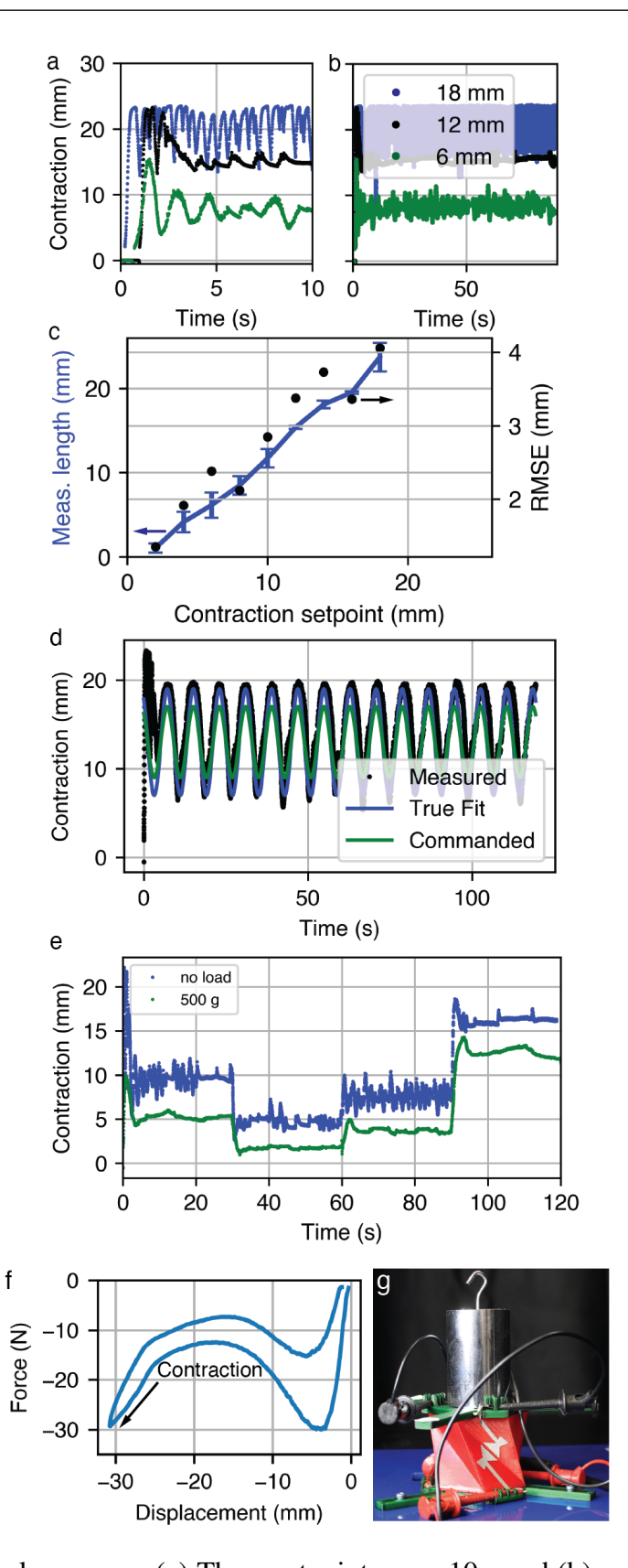


Figure 7. Feedback control response. (a) Three setpoints over 10 s and (b) over 90 s. (c) The actuator length across three trials and RMSE. (d) The response to a commanded sinusoidal input with the true fit representing a sinusoidal fit to the measured data and (e) control input steps for weighted and unweighted conditions at 8 mm, 4 mm, 6 mm, and 12 mm. (f) The force-displacement curve for a single Kresling unit. (g) A photograph of a single Kresling robot under a 500 g load during a position tracking test.

by using a set of capacitive sensors on the top or bottom unit to estimate length and rotation of each unit and determine PWM input. Three target contractions and top face angles were set: $L_{2DOF}=68$ mm, such that the contracted length is 14 mm and $\alpha_{2DOF}=0^{\circ}$, and $L_{2DOF}=75$ (7 mm contraction) with $\alpha_{2DOF}=-16.5^{\circ}$ and $\alpha_{2DOF}=+16.5^{\circ}$.

Fig. 8 is a plot of top face rotation and contraction for each commanded pose. In the first target conditions, the position overshoots before settling to its final value with contraction and angle RMSE of 3.6 mm and 13.6°, respectively, 30 s after the start of the test. In the second and third target conditions, the robot has contraction RMSE of 0.5 mm and 1.7 mm, respectively, with angle RMSE of 3.5° and 6.1°.

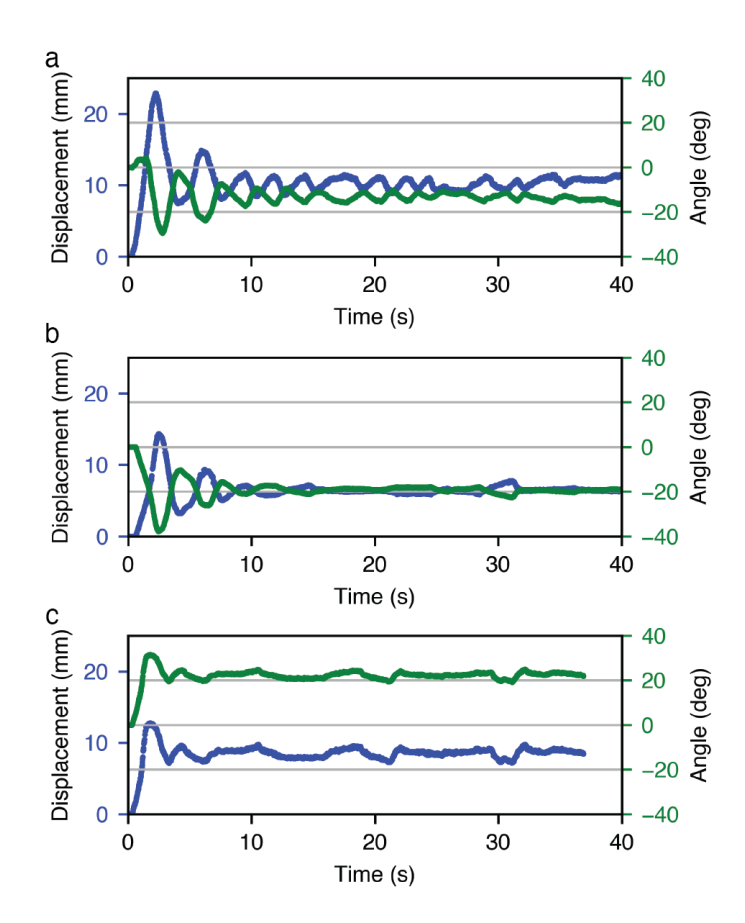


Figure 8. Feedback control response of the double Kresling robot, with target setpoints for contraction and α of (a) 14 mm and 00° (b) 7 mm and -16° (c) 7 mm and +16°.

6 DISCUSSION

297

298

299

300

301

302

303

304

305

293

294

295

296

The Kresling structure offers a rich testbed for investigating proprioceptive sensor performance in a soft robot. Integration of capacitive sensors onto the Kresling body permitted position control for contraction setpoints up to 17 mm, or 41% of the total robot length, with RMSE below 3 mm for setpoints less than 10 mm and below 4 mm for all setpoints. One source of error was the mapping from capacitance to length. The linear relationship observed in Fig. 7c between length and setpoint has a slope higher than one, or a higher estimate of contraction. Increasing scale factor κ may improve position estimation.

We demonstrated that the triangle electrode had higher sensitivity than the optimized OC5 electrode but was not robust to repeated actuation. We attribute this performance to the mismatch between electrode strain and Kresling strain, particularly at the corners. The actuator visibly twists and stretches, causing

the inextensible electrodes to delaminate. The OC5 electrodes are placed on regions of the sidewalls that remain relatively planar and unstretched, with only small concavity when a vacuum is introduced. This smaller deformation reduces the likelihood of delamination.

The sensitivities of each optimized electrode OC1-OC5 were on the same order of magnitude. We hypothesize that OC 5 was the optimal shape from the five electrodes due to lower capacitance at full contraction rather than higher capacitance at full extension. The small performance increase over the hexagon (OC1) and the inverted triangle (OC4) suggest that any electrode with sufficiently large sensitivity over the noise floor and located far from the triangular face corners may be suitable for closed-loop control.

Increasing setpoint beyond 17 mm of contraction caused instability, which is visible in Fig. 7a as rapid oscillation around the setpoint. At this distance, the known bistable-like properties of the Kresling structure cause the robot to rapidly undergo a change in state for which the controller cannot compensate. Overshooting the setpoint causes the electrodes to make momentary contact, which results in maximum capacitance readings and therefore erroneously calculated short lengths. The system overcompensates as it perceives a much larger error than is present. This behavior is present in the first few seconds of the sinusoid following in Fig. 7e. It follows a cyclic pattern; however, at larger contraction amplitudes, the system must overcome both the elastic restoring force present when the Kresling contracts to reach the set point and generates overshoot. To avoid this error in practice, we may simply restrict the contraction range of the contraction below 17 mm, thus preventing rapid change, overshoot, and contact.

The single-unit Kresling robot is able to withstand forces up to 30 N before full contraction, and the force-displacement curve demonstrates similar non-linear stiffness to behavior observed in Kresling robots fabricated from polymer films Bhovad et al. (2019). Of note, due to strain energy stored in the TPU during contraction, there is no bistable point. This is a critical difference in this Kresling fabricated from an elastomer and previous observations of Kreslings fabricated in paper or polymer films.

The robot does demonstrate larger position error under load than without, and it undershoots the position target (i.e., less contraction than without the mass). Interestingly, this behavior opposes the expectation for an additional compressive force acting on the mass, i.e., the contraction should increase rather than decrease. We hypothesize that the response and decreased contraction is due to the large nearby metal, which will distort the relationship between capacitance and contraction. This response motivates further investigation of passive and active shielding approaches that screen the influence of the surrounding environment from the capacitive sensors.

We established the ability to independently control robot length and top face rotation using sets of capacitive electrodes on the top and bottom Kresling units. The contraction setpoint errors were in line with the results observed from the single-unit Kresling error (3.6 mm vs. 3.4 mm, respectively at 14 mm contraction), and the angle errors for one actuated unit within the two-unit robot were slightly larger (3.5° and 6.1° vs. 2.1°) than for the single-unit Kresling. The angle error for the two-unit Kresling when both the top and bottom units were actuated was appreciably larger (13.6°). During actuation, the bottom Kresling appears to tilt and twist when the top Kresling unit is actuated. This behavior may be attributed to a non-ideality in the bottom unit sidewall thickness that creates bending under actuation.

The nonlinear capacitance-length relationship, non-rigid deformation, and bi-stable behavior add complexity to feedback control and provide additional motivation for feedback control over open-loop control. While open-loop control is more common in soft robotics, it also requires a much finer degree of system identification for accurate control. Therefore, we view proprioceptive feedback as a crucial capability for emerging soft robotics.

7 CONCLUSIONS

- 349 Applying proprioceptive position sensing to control actuator position is an ongoing challenge in soft
- 350 robotics. To address this challenging problem, we demonstrated a Kresling origami-inspired, 3D printed,
- 351 fluidically actuated robot with capacitive sensors integrated onto the sidewall faces. Through optimizing
- 352 the geometry of the capacitive electrodes, we maximized the sensitivity at large fold angles. The observed
- 353 kinematics of the Kresling rotation and contraction show strong agreement with a linear model of changing
- 354 capacitance along the sidewall folds. We demonstrated the utility of our sensing and modeling to achieve
- 355 varying conformal states of the Kresling along its range of motion.
- We further demonstrated the ability to transition between setpoint states and achieved less than 4 mm
- 357 setpoint error across a setpoint to 17 mm. This minimized error allowed us to achieve complex motion
- 358 patterns such as tracking a sine wave. We also observed the Kresling performance to achieve desired
- 359 contraction under external loading. The success of the 1DOF control was expanded to a 2DOF system of
- 360 stacked Kreslings, where we achieved independent control of contraction and rotation angle.
- 361 This work constitutes a significant step towards reliable, low-cost proprioceptive sensing for origami robots.
- 362 Building on the 2DOF robot, we intend to explore the pantheon of achievable robot morphologies by
- 363 using the Kresling as the base unit. This will include actuators with controllable bending. Joining several
- 364 sensorized Kresling structures will enable complex motion strategies that include crawling and movement
- 365 in 6-DOF pose space. Other areas of future work include improving the electrode design and manufacturing,
- 366 fabrication approaches to reduce capacitance variations between electrode pairs, and investigating different
- 367 control approaches. Future research in multi-Kresling robots will also explore passive and active shielding
- 368 approaches in future work to reduce environmental interference in the electrodes.
- 369 The results of this work demonstrate that capacitive sensing is a promising and adaptable technique for
- 370 proprioceptive state estimation in soft robotics.

CONFLICT OF INTEREST STATEMENT

- 371 The authors declare that the research was conducted in the absence of any commercial or financial
- 372 relationships that could be construed as a potential conflict of interest.

AUTHOR CONTRIBUTIONS

- 373 N. Hanson: formal analysis, investigation, software, visualization, writing; I. Ampomah: investigation,
- 374 software, writing; S. Roberts: conceptualization, investigation, methodology, software, visualization,
- 375 writing; J. Healey: Investigation, software, writing; C. Wu: investigation, writing; K. Dorsey:
- 376 conceptualization, funding, formal analysis, investigation, methodology, supervision, visualization, writing.

FUNDING

This work is supported by NSF CAREER 1846954.

ACKNOWLEDGMENTS

- 378 The authors thank A. Allison, S. Alt, and G. Lvov for assistance with experimental setup and 3D printing,
- 379 and T. Padir for use of the Optitrack system.

DATA AVAILABILITY STATEMENT

380 Project code, materials list, and assembly instructions are available online: https://parses-lab.

381 github.io/kresling_control/

REFERENCES

- Babu, S. P. M., Das, R., Mazzolai, B., and Rafsanjani, A. (2023). Programmable inflatable origami. In 2023 IEEE International Conference on Soft Robotics (RoboSoft) (IEEE), 1–6
- 384 Best, C. M., Gillespie, M. T., Hyatt, P., Rupert, L., Sherrod, V., and Killpack, M. D. (2016). A new soft
- robot control method: Using model predictive control for a pneumatically actuated humanoid. *IEEE*
- 386 Robotics & Automation Magazine 23, 75–84
- 387 Bhovad, P., Kaufmann, J., and Li, S. (2019). Peristaltic locomotion without digital controllers: Exploiting
- multi-stability in origami to coordinate robotic motion. Extreme Mechanics Letters 32, 100552
- 389 [Dataset] Bovbel, P. (2017). Vrpn client ros
- 390 Chen, Q., Feng, F., Lv, P., and Duan, H. (2022). Origami spring-inspired shape morphing for flexible
- 391 robotics. *Soft Robotics* 9, 798–806
- 392 Della Santina, C., Katzschmann, R. K., Biechi, A., and Rus, D. (2018). Dynamic control of soft robots
- interacting with the environment. In 2018 IEEE International Conference on Soft Robotics (RoboSoft).
- 394 46–53. doi:10.1109/ROBOSOFT.2018.8404895
- 395 Dong, H., Yang, H., Ding, S., Li, T., and Yu, H. (2022). Bioinspired amphibious origami robot with body
- sensing for multimodal locomotion. *Soft Robotics* 9, 1198–1209
- 397 Dorsey, K. L., Huang, H., and Wen, Y. (2022). Origami-patterned capacitor with programmed strain
- sensitivity. *Multifunctional Materials* 5, 025001
- 399 Firouzeh, A. and Paik, J. (2015). Robogami: A fully integrated low-profile robotic origami. *Journal of*
- 400 Mechanisms and Robotics 7, 021009
- 401 Hawkes, E. W., Majidi, C., and Tolley, M. T. (2021). Hard questions for soft robotics. Science robotics 6,
- 402 eabg6049
- 403 Huang, J., Zhou, J., Wang, Z., Law, J., Cao, H., Li, Y., et al. (2022). Modular origami soft robot with the
- perception of interaction force and body configuration. Advanced Intelligent Systems 4, 2200081
- 405 Kaufmann, J., Bhovad, P., and Li, S. (2022). Harnessing the multistability of kresling origami for
- reconfigurable articulation in soft robotic arms. Soft Robotics 9, 212–223
- 407 Kim, T.-H., Bao, C., Chen, Z., and Kim, W. S. (2022). 3d printed leech-inspired origami dry electrodes for
- 408 electrophysiology sensing robots. NPJ Flexible Electronics 6, 5
- 409 Kim, T.-H., Vanloo, J., and Kim, W. S. (2021). 3d origami sensing robots for cooperative healthcare
- 410 monitoring. Advanced Materials Technologies 6, 2000938
- 411 Kresling, B. (2012). Origami-structures in nature: lessons in designing "smart" materials. MRS Online
- 412 Proceedings Library (OPL) 1420, mrsf11–1420
- 413 Lagarias, J. C., Reeds, J. A., Wright, M. H., and Wright, P. E. (1998). Convergence properties of the
- 414 nelder–mead simplex method in low dimensions. SIAM Journal on optimization 9, 112–147
- 415 Li, J., Godaba, H., Zhang, Z., Foo, C., and Zhu, J. (2018). A soft active origami robot. Extreme Mechanics
- 416 *Letters* 24, 30–37
- 417 Li, S., Stampfli, J. J., Xu, H. J., Malkin, E., Diaz, E. V., Rus, D., et al. (2019). A vacuum-driven origami
- "magic-ball" soft gripper. In 2019 International Conference on Robotics and Automation (ICRA) (IEEE),
- 419 7401–7408

Mori, T. and Onoe, H. (2021). Shape-recognizable origami sheet device with single walled carbon nanotube strain sensor. *Journal of Microelectromechanical Systems* 30, 234–242

- 422 Nisser, M. E. W., Felton, S. M., Tolley, M. T., Rubenstein, M., and Wood, R. J. (2016). Feedback-controlled
- self-folding of autonomous robot collectives. In 2016 IEEE/RSJ International Conference on Intelligent
- 424 Robots and Systems (IROS). 1254–1261. doi:10.1109/IROS.2016.7759208. ISSN: 2153-0866
- Pagano, A., Yan, T., Chien, B., Wissa, A., and Tawfick, S. (2017). A crawling robot driven by multi-stable origami. *Smart Materials and Structures* 26, 094007
- Park, Y., Kang, J., and Na, Y. (2022). Reconfigurable shape morphing with origami-inspired pneumatic blocks. *IEEE Robotics and Automation Letters* 7, 9453–9460
- 429 Patterson, Z. J., Sabelhaus, A. P., Chin, K., Hellebrekers, T., and Majidi, C. (2020). An Untethered Brittle
- 430 Star-Inspired Soft Robot for Closed-Loop Underwater Locomotion. In 2020 IEEE/RSJ International
- 431 Conference on Intelligent Robots and Systems (IROS). 8758–8764. doi:10.1109/IROS45743.2020.
- 432 9341008. ISSN: 2153-0866
- 433 Quigley, M., Conley, K., Gerkey, B., Faust, J., Foote, T., Leibs, J., et al. (2009). Ros: an open-source robot operating system. In *ICRA workshop on open source software* (Kobe, Japan), vol. 3, 5
- Robertson, M. A., Kara, O. C., and Paik, J. (2021). Soft pneumatic actuator-driven origami-inspired modular robotic "pneumagami". *The International Journal of Robotics Research* 40, 72–85
- Seeger, J. I. and Boser, B. E. (2003). Charge control of parallel-plate, electrostatic actuators and the tip-in instability. *Journal of Microelectromechanical systems* 12, 656–671
- Shih, B., Shah, D., Li, J., Thuruthel, T. G., Park, Y.-L., Iida, F., et al. (2020). Electronic skins and machine learning for intelligent soft robots. *Science Robotics* 5, eaaz9239
- Sun, Y., Li, D., Wu, M., Yang, Y., Su, J., Wong, T., et al. (2022a). Origami-inspired folding assembly of dielectric elastomers for programmable soft robots. *Microsystems & Nanoengineering* 8, 37
- Sun, Y., Wang, J., and Sung, C. (2022b). Repeated jumping with the rebound: Self-righting jumping robot leveraging bistable origami-inspired design. In 2022 International Conference on Robotics and
- 445 *Automation (ICRA)* (IEEE), 7189–7195
- Tapia, J., Knoop, E., Mutnỳ, M., Otaduy, M. A., and Bächer, M. (2020). Makesense: Automated sensor
 design for proprioceptive soft robots. *Soft robotics* 7, 332–345
- Thuruthel, T. G., Shih, B., Laschi, C., and Tolley, M. T. (2019). Soft robot perception using embedded soft sensors and recurrent neural networks. *Science Robotics* 4, eaav1488
- 450 Wang, Z., Wu, H., Feng, Z., and Wang, H. (2022). A stick on, film-like, split angle sensor via magnetic
- induction for versatile applications. *IEEE Transactions on Instrumentation and Measurement* 71, 1–9
- 452 Williams, S. R., Suchoski, J. M., Chua, Z., and Okamura, A. M. (2022). A 4-Degree-of-Freedom Parallel
- 453 Origami Haptic Device for Normal, Shear, and Torsion Feedback. *IEEE Robotics and Automation Letters*
- 454 7, 3310–3317. doi:10.1109/LRA.2022.3144798. Conference Name: IEEE Robotics and Automation
- 455 Letters
- 456 Wu, S., Ze, Q., Dai, J., Udipi, N., Paulino, G. H., and Zhao, R. (2021). Stretchable origami robotic arm
- with omnidirectional bending and twisting. *Proceedings of the National Academy of Sciences* 118,
- 458 e2110023118
- 459 Yan, W., Li, S., Deguchi, M., Zheng, Z., Rus, D., and Mehta, A. (2023). Origami-based integration of
- robots that sense, decide, and respond. *Nature Communications* 14, 1553
- 461 Ze, Q., Wu, S., Nishikawa, J., Dai, J., Sun, Y., Leanza, S., et al. (2022). Soft robotic origami crawler.
- 462 Science advances 8, eabm7834